VERIFICATION OF ORTHORHOMBIC ANISOTROPY BY DIRECT MODELING OF SEISMIC DATA OF THE NEUQUÉN BASIN, ARGENTINA

Sergio A. Sosa[1], Juan I. Sabbione[2], Mauricio D. Sacchi[3]

1: Seismic Prospect S.R.L. and Facultad de Ciencias Exactas y Tecnología, Universidad Nacional de Tucumán.
ssosa@seismicprospect.com

2: Facultad de Ciencias Astronómicas y Geofísicas, Universidad Nacional de La Plata and CONICET.
jsabbione@fcaglp.unlp.edu.ar

3: Department of Physics, University of Alberta. msacchi@ualberta.ca

Keywords: Seismic Modeling, Orthorhombic Anisotropy, Vaca Muerta Formation, Imaging

RESUMEN

El procesamiento y el análisis de dato sísmico de la Cuenca Neuquina es complejo porque la propagación de ondas en un medio anisotrópico influye en la estimación de velocidades y en el proceso de migración, incluso en las zonas estructuralmente simples desde el punto de vista de sus buzamientos. La estimación de los parámetros que controlan la propagación anisotrópica de las ondas es crucial para obtener imágenes de alta resolución e integrar el dato sísmico a estudios geomecánicos y de caracterización de reservorios. Proponemos un flujo de procesamiento para explicar los patrones del moveout que caracterizan al dato sísmico adquirido en el Engolfamiento de la Cuenca Neuquina. El flujo se basa en tres etapas fundamentales. Primero, los parámetros anisotrópicos son estimados del dato real. Luego, los mismos se emplean para crear respuestas sísmicas sintéticas 3D para los modelos isotrópico, anisotrópico VTI y anisotrópico ortorrómbico. El proceso concluye con una comparación de los gathers sintéticos y reales. Esta etapa se complementa con un análisis estadístico de las correcciones de moveout residuales calculadas por correlación cruzada. Se demuestra que un modelo ortorrómbico explica, predominantemente, la propagación de ondas acústicas en el área de estudio, con una incidencia influyente en formaciones típicas de interés en esta cuenca (Quintuco y Vaca Muerta). Por lo tanto, en futuras investigaciones debería realizarse un modelado 3D más exhaustivo para cuantificar el impacto de la anisotropía ortorrómbica en las imágenes sísmicas.

INTRODUCTION

The Embayment of the Neuquén Basin is characterized by a demonstrated vertical anisotropy (VTI) (Curia *et al.*, 2016; Sagasti *et al.*, 2014), in particular when structural dips have not a significant influence. For more complex structures, this situation converges to a tilted anisotropy (TTI) behavior of the seismic waves. This work is focused on the former and simpler situation. In addition, a large extension of the basin is influenced by a dominant stress pattern orientation. The first-order maximum horizontal stress is close to the west-east direction. This fact was regionally demonstrated by borehole breakout analysis (Guzmán *et al.*, 2007). In more localized studies, vertical seismic profiles (Curia *et al.*, 2016) or seismic inversion case studies (Benítez, 2019; Curia *et al.*, 2018; Soldo *et al.*, 2017) arrived to the same conclusion. As a consequence, seismic P-waves are also influenced by horizontal anisotropy (HTI). The combination of the VTI and HTI behaviors leads to an orthorhombic (ORT) model (Grechka and Tsvankin, 1999; Tsvankin, 1997). This fact has been previously identified (Muzzio and María, 2018; Holcombe *et al.*, 2014) and also measured using traveltimes signatures in seismic data from the Neuquén Basin area (Sosa and Volonté, 2019). This scenario suggests conducting a formal 3D geophysical forward modeling study aimed to demonstrate that observed traveltimes signatures are linked to the described orthorhombic context. Additionally, such study would allow to describe how these signatures can be exhaustively exploited to estimate the involved anisotropic parameters.

Input data are pre-image gathers, VTI PSTM gathers and VTI PSDM products from a 3D seismic data located on the north-west of the Embayment of the Neuquén Basin. The modeling study is restricted to five characteristic locations of the full Seismic Area (Fig. 1). The acquisition patch includes azimuths from 0 to 360°, with offset components ranging from 0 to 3800 m in

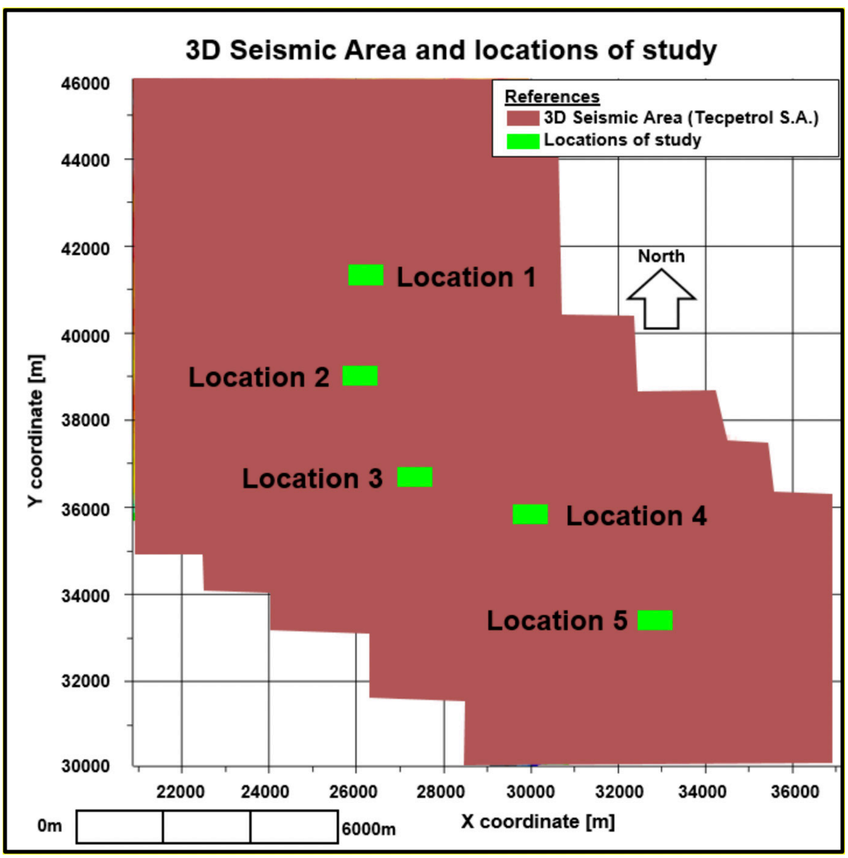

Figure 1. 3D Seismic Area and locations of study.

the north-south direction and from 0 to 7500 m in the west-east direction. Additionally, it is significant to remark that structural geological dips are lower than 5°.

METHODOLOGY

Background and objectives

Preconditioned COCA (Common Offset – Common Azimuth) gathers for imaging in the Embayment of the Neuquén Basin show a characteristic moveout pattern associated with the azimuth of wave propagation as shown in Figure 2. They are particularly evident on high amplitude reflectors, as for instance the top of the Rayoso formation (horizon A), the top of the Quintuco formation (horizon B) or the base of the Vaca Muerta formation. Additionally, estimated incidence angles on these horizons show a favorable situation to evaluate anisotropic effects. Consequently, these reflectors play a significant role on the orthorhombic parameters estimation method that is explained later in this work.

If analyzed locally, those moveout patterns could be associated with lateral changes of static corrections that are not fully modeled at this stage. However, this interpretation shall be discarded because surface consistent residual static corrections are iterated until they converge to values lower than the time range of these patterns. Alternatively, they could be linked to lateral changes of velocities, which would be consistent with the presence of these patterns even after VTI PSTM (Fig. 2). This imaging technique does not account for lateral variation of velocities. Nonetheless, after analyzing average residual moveout corrections on VTI PSTM gathers computed via cross-correlation in the full area (Fig. 3), it is concluded that these patterns are associated with a regional phenomenon. Traveltimes are systematically lower in the west-east direction, where first-order maximum horizontal stress is expected (Guzmán *et al.*, 2007). Consequently, most of this residual moveout related with the azimuth can be justified by a horizontal anisotropic model (HTI). Finally, when added to a VTI context as is expected for a sedimentary context with low dips, the orthorhombic anisotropic model is assumed as the most probable hypothesis of this work.

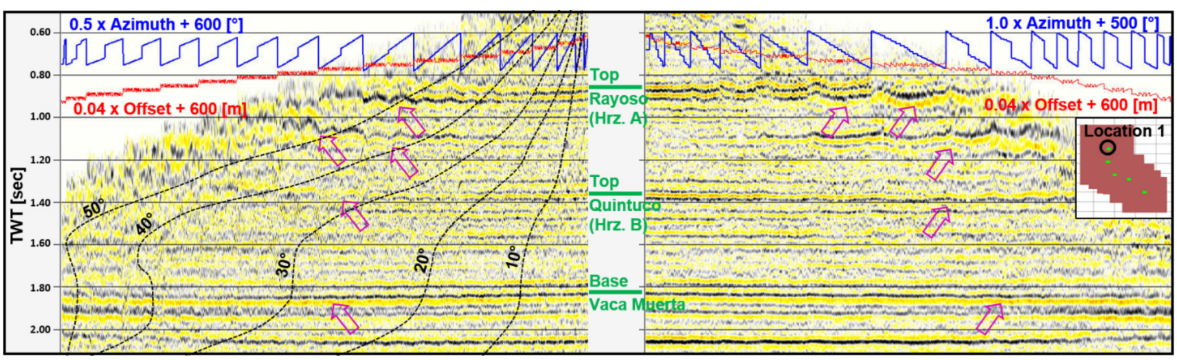

Figure 2. COCA gathers from Location 1. Input to VTI PSTM – Incidence angles estimation (left). Output from VTI PSTM (right).

Our first goal is to demonstrate that a flat model without lateral changes of static corrections and velocities can produce synthetic unmigrated gathers that match the moveout patterns observed in the real data only by modifying its anisotropic properties. The second goal is to demonstrate

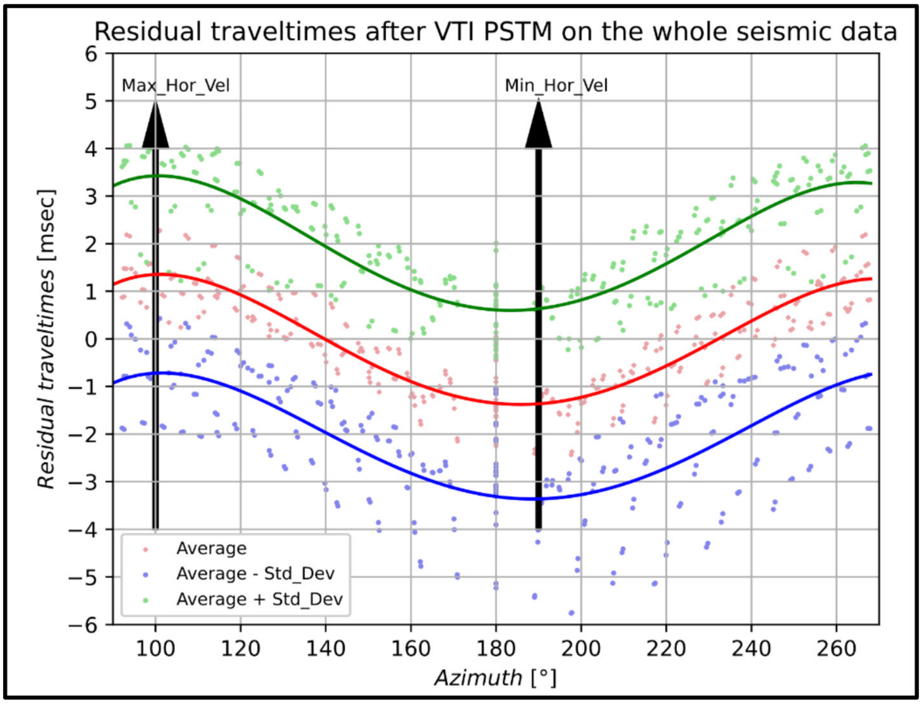

Figure 3. Residual traveltimes measured on the whole seismic data after VTI PSTM. Traveltimes are averaged on each migration plane. The offset trend is removed using a fourth-degree polynomial fit.

that the orthorhombic parameters can be accurately estimated from the real seismic data.

Isotropic and VTI models building

We built one velocity model in depth for each location shown in Figure 1 using the best estimation obtained from the available VTI PSDM products. The interval vertical velocity VPz for each location is extracted from the corresponding cube and then propagated to the full area. Regarding the topographic surface, its value is constant and equal to the real elevation at each location. Figure 4 shows the isotropic V_{Pz} model for Location 1.

In terms of anisotropic parameters, it is desirable to find single representative estimations for the whole area in order to understand the regional behavior of the residual moveout (Fig. 3). For the VTI models it is enough to estimate the interval VTI Thomsen parameters delta (δ) and epsilon (ε) in depth. The first step is to generate tridimensional semblances in the time domain

(Neidell and Taner, 1971) from VTI PSTM gathers on a 1 km by 1 km grid. RMS normal moveout velocities ($V_{P\ nmo\ rms}$) are measured on these semblances (Fig. 5) to correct for normal moveout for incidence angles up to 25°, while effective anisotropy etas (η_{eff}) are used to correct angles higher than 25°. Both medium properties are related to δ and ε (Alkhalifah, T., and Tsvankin, I., 1995). Relevant relationships are

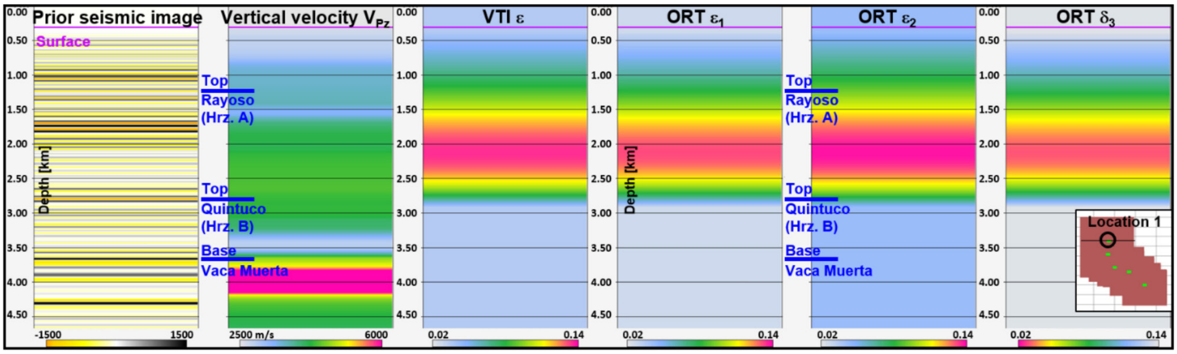

Figure 4. Models sections for Location 1. From left to right: prior image, V_{Pz}, VTI ε, ORT ε_1, ORT ε_2, and ORT δ_3.

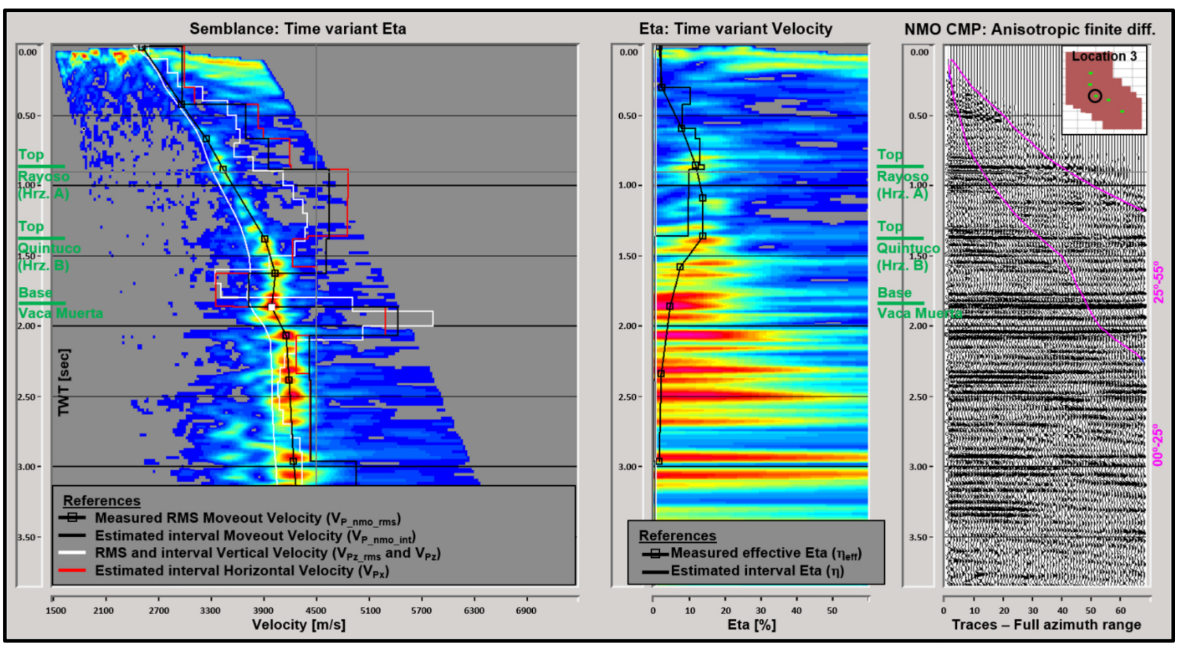

Figure 5. Tridimensional semblance to measure RMS normal moveout velocities and effective anisotropy.

$$V_{P\_nmo} = V_{Pz}\sqrt{1+2\delta},$$
$$\varepsilon = \delta + \eta + 2\delta\eta.$$

RMS normal moveout velocities are transformed to interval velocities in depth ($V_{P\_nmo\_int\_}$

depth) (Dix, 1955) from the seismic time reference surface scaled to depth (Sosa and Volonté, 2017). Figure 6 illustrates the matching between the average of these estimations and the vertical velocities from calibrated and smoothed P-sonic logs. Trends are comparable from the surface to the top of the Quintuco formation. In this range, $V_{P\ nmo\ int\ depth}$ is an overestimation of V_{Pz}, meaning a positive δ. A general assessment of this difference offers a way to estimate δ. An interpretation in time of the top of the Quintuco marker is stretched to depth using seismic velocities $V_{P\ nmo\ int\ depth}$ (Z_{nmo}) and PSDM velocities V_{Pz} calibrated with well markers (Z_z). Using equation 1 and approximating $\sqrt{1+2\delta}$ via a binomial expansion up to the second term, the average relative depth difference between both surfaces produces a global reasonable estimation for interval δ, because

$$\frac{Z_{nmo}-Z_z}{Z_z}=\frac{Z_{nmo}}{Z_z}-1=\frac{t\,V_{P\_nmo}}{t\,V_{Pz}}-1=\frac{V_{Pz}\sqrt{1+2\delta}}{V_{Pz}}-1=\sqrt{1+2\delta}-1\cong 1+\frac{1}{2}2\delta-1=\delta. \quad (3)$$

Once estimated in the full area of coverage, the average interval value of δ is equal to 0.035 (Fig. 7). An average function of the effective anisotropy η_{eff} functions measured in the whole area is computed and transformed to interval η in time. Using equation 2, interval δ and η can be used to compute interval ε in time (Fig. 8). Finally, both functions δ and ε are converted to depth using the isotropic velocity model from each location to build the VTI models. Figure 4 shows a ε section in depth for Location 1.

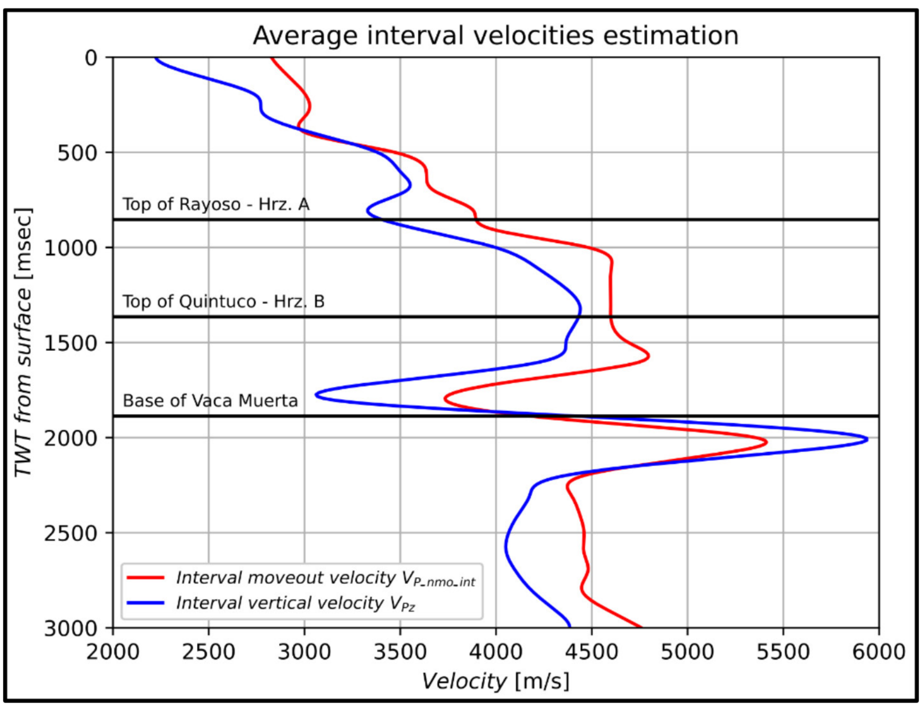

Figure 6. Average interval velocities estimation.

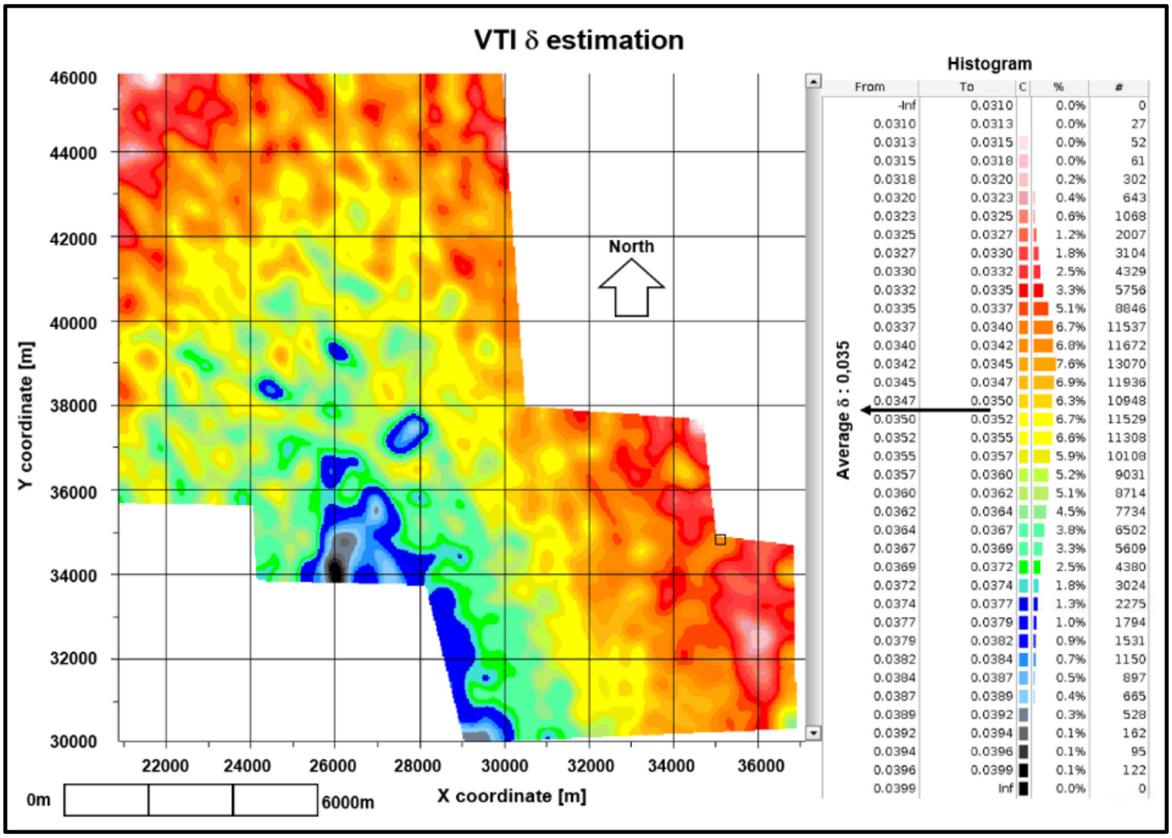

Figure 7. VTI δ estimation.

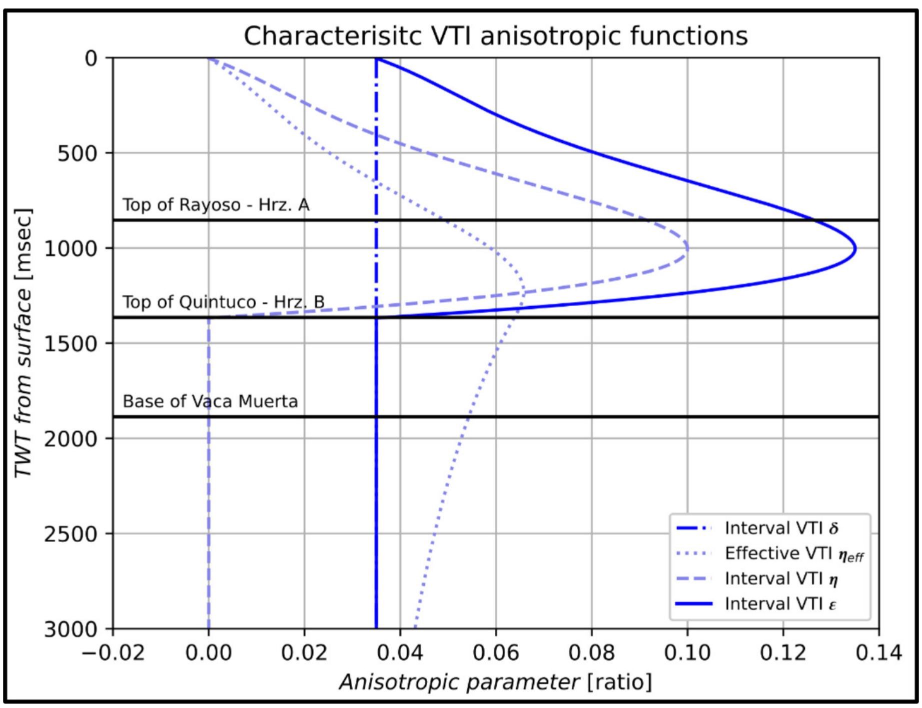

Figure 8. Characteristic VTI anisotropic functions.

Orthorhombic (ORT) models building

Kinematic signatures of P-waves in weakly anisotropic orthorhombic media depend on five anisotropic coefficients, on the direction of maximum horizontal velocity V_{Ph} and on the vertical velocity V_{Pz} (Tsvankin, 1997). The phase velocity of P-waves has the same mathematical representation as in VTI media (Thomsen, 1986), but with azimuthally dependent coefficients δ and ε (Tsvankin, 1997). In the following equation, the sub index (i = 1) corresponds to the direction of minimum horizontal velocity, while (i = 2) is related to the direction of maximum horizontal velocity (α)

$$V_P(\theta,\phi) = V_{Pz}(1 + \delta(\phi)\sin^2\theta\cos^2\theta + \varepsilon(\phi)\sin^4\theta) \quad (4)$$

$$\delta(\phi) = \delta_1\sin^2\phi + \delta_2\cos^2\phi \quad (5)$$

$$\varepsilon(\phi) = \varepsilon_1\sin^4\phi + \varepsilon_2\cos^4\phi + (2\varepsilon_2 + \delta_3)\sin^2\phi\cos^2\phi, \quad (6)$$

where θ is the angle of incidence and ϕ is the difference between the direction of maximum horizontal velocity (α) and the azimuth of propagation. The coefficient δ_3 plays the role of Thomsen's δ in VTI equations written for the (x1, x2) symmetry plane, with the x1-direction replaced by the symmetry axis (Tsvankin, 1997).

In conclusion, seven parameters must be estimated to build the ORT models: V_{Pz}, α, δ_1, δ_2, ε_1, ε_2, and δ_3. First, the vertical velocity V_{Pz} is taken from the isotropic model. Second, a fourth degree polynomial curve is fitted to the average residual traveltimes (Fig. 3). Then, the position in the horizontal axis of the maximum value is the direction of maximum horizontal velocity α that is close to 100°. This result is consistent with regional maximum stresses expected in the area accordingly to the most recent version of the world stress map database (Heidbach *et al.*, 2016). The nearest record of this database is about 27 km away from the area of study in the west direction. Its identification code is wsm14653 and the measured azimuth of the maximum stress direction is 106° with a standard deviation of 28°.

The next step is to find statistical evidence about the parameters δ_1, δ_2, ε_1, and ε_2. Initially, two sets of tridimensional semblances are generated in the time domain from VTI PSTM gathers on a 1 km by 1 km grid. The first set is approximately oriented along the direction of the minimum horizontal velocity (α + 90°), using seismic traces with azimuths ranging from 170° to 210° (Fig. 9). The second set is approximately oriented along the direction of the maximum horizontal velocity (α ≅ 100°) with azimuths in the range 80° to 120° (Fig. 10). These semblances, as in the VTI case, give information about the optimum combination of $V_{P\_nmo\_rms\_i}$ and η_{eff_i} to enhance the stack energy, where the index i represents the analysis direction.

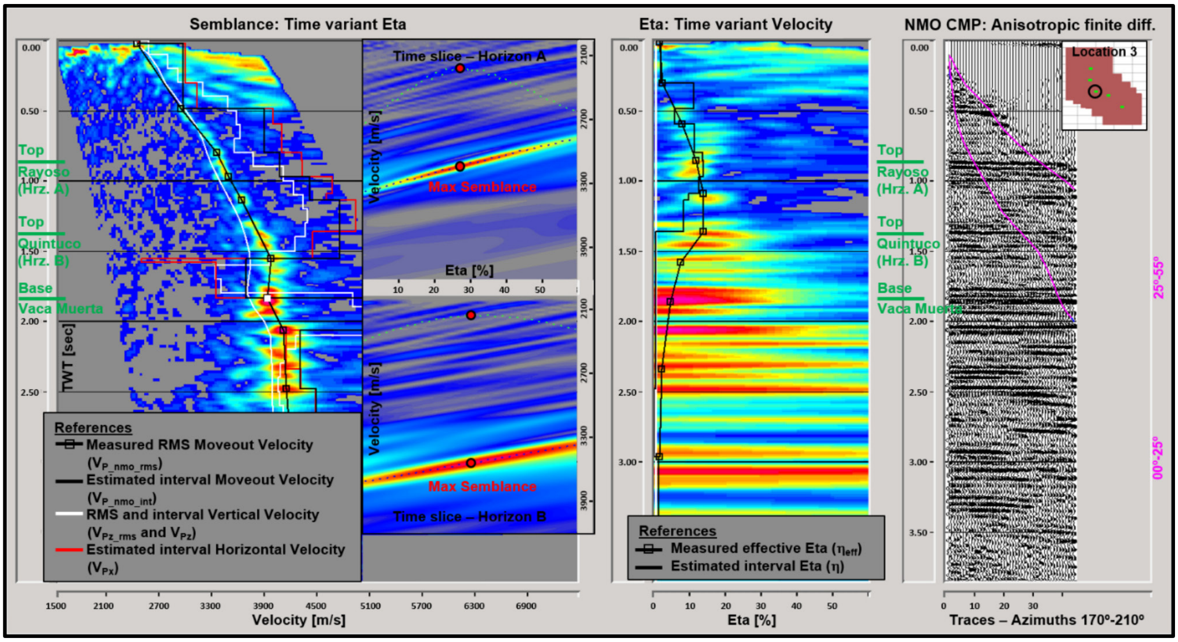

Figure 9. Tridimensional semblance to measure RMS normal moveout velocities and effective anisotropy. Seismic traces with azimuths around the direction of the minimum V_{Ph}. Horizon consistent automatic semblance analysis.

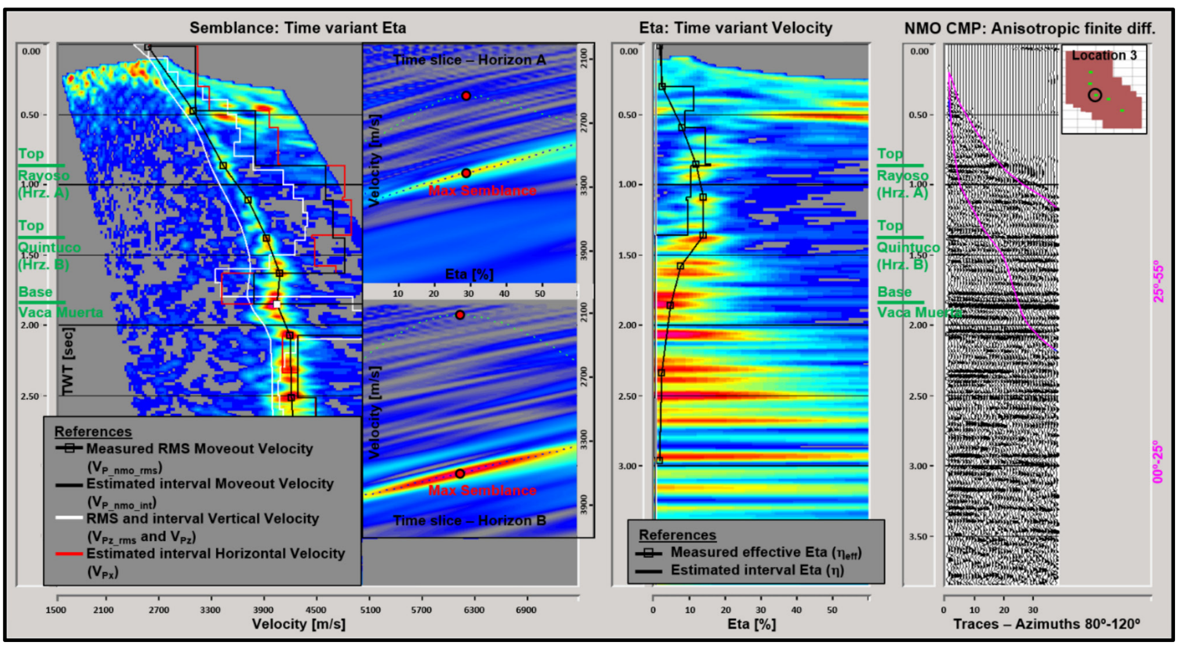

Figure 10. Tridimensional semblance to measure RMS normal moveout velocities and effective anisotropy. Seismic traces with azimuths around the direction of the maximum V_{Ph}. Horizon consistent automatic semblance analysis.

This azimuthal analysis method and similar approaches have been employed by several authors to find evidence about horizontal velocities changes that are afterwards used for residual normal moveout corrections or imaging strategies (Hilburn *et al.*, 2017; Xie *et al.*, 2012; Li *et al.*, 2012; Jenner, 2011). In this case, the goal is to develop a statistical method that allows both to identify and quantify those changes and to fit them to the mathematical and physical model suggested by equation 4 (Tsvankin, 1997). In this way, this method pursues an accurate and physically meaningful estimation of δ_1, δ_2, ε_1, ε_3 and δ_3 for the Embayment of the Neuquén Basin, within the limitations of the available seismic data.

Then, computed semblances are automatically analyzed on time slices corresponding to the time position of the horizon A and horizon B, where the orthorhombic phenomenon is better identified. On each time slice, all η_{eff} values are scanned to find the pair ($V_{P\ nmo\ rms}$, S) where the semblance S takes the highest value. Pairs (η_{eff}, S) are fitted to a polynomial curve of third degree. This function is differentiated to get the η_{eff} position of the maximum S (S_{max}). Then, the linear trend of the (η_{eff}, $V_{P\ nmo\ rms}$) pairs is computed and used for obtaining the $V_{P\ nmo\ rms}$ position of the maximum semblance S_{max} (Figs. 9 and 10). This analysis is carried out for a total of 164 locations, on 2 time slices and for 2 azimuth sectors, getting an analytical estimation of the pair (η_{eff}, $V_{P\ nmo\ rms}$) where the maximum semblance S_{max} is located for each particular situation.

Using equation 1, and assuming that the average of $V_{P\ nmo\ rms\ 1}$ and $V_{P\ nmo\ rms\ 2}$ provides a reasonable estimation of $V_{P\ nmo\ rms}$, then

$$V_{P\_nmo\_rms} = \frac{V_{P\_nmo\_rms\_1} + V_{P\_nmo\_rms\_2}}{2} = V_{Pz\_rms}\sqrt{1 + 2\delta_{eff}}, \tag{7}$$

thus,

$${V_{Pz\_rms}}^2 = \frac{\left(V_{P\_nmo\_rms\_1} + V_{P\_nmo\_rms\_2}\right)^2}{4\left(1 + 2\delta_{eff}\right)}. \tag{8}$$

Applying equation 1 for the minimum and maximum horizontal velocities directions

$$\begin{aligned} {V_{P\_nmo\_rms\_1}}^2 &= {V_{Pz\_rms}}^2\left(1 + 2\delta_{eff\_1}\right), \qquad (9)\\ {V_{P\_nmo\_rms\_2}}^2 &= {V_{Pz\_rms}}^2\left(1 + 2\delta_{eff\_2}\right). \qquad (10)\end{aligned}$$

Subtracting 9 from 10 and using 8

$$\delta_{eff\_2} - \delta_{eff\_1} = \frac{{V_{P\_nmo\_rms\_2}}^2 - {V_{P\_nmo\_rms\_1}}^2}{{V_{Pz\_rms}}^2} = 4\left(1 + 2\delta_{eff}\right)\frac{{V_{P\_nmo\_rms\_2}}^2 - {V_{P\_nmo\_rms\_1}}^2}{\left(V_{P\_nmo\_rms\_1} + V_{P\_nmo\_rms\_2}\right)^2}. \tag{11}$$

Since δ does not change vertically in the proposed models, the effective property is equal to the interval property. Furthermore, from the VTI model we know that $\delta_{eff} = 0.035$. Consequently

$$\delta_2 - \delta_1 = 4(1 + 2\delta)\frac{{V_{P\_nmo\_rms\_2}}^2 - {V_{P\_nmo\_rms\_1}}^2}{\left(V_{P\_nmo\_rms\_1} + V_{P\_nmo\_rms\_2}\right)^2} = 4(1 + 2 \times 0.035)\frac{{V_{P\_nmo\_rms\_2}}^2 - {V_{P\_nmo\_rms\_1}}^2}{\left(V_{P\_nmo\_rms\_1} + V_{P\_nmo\_rms\_2}\right)^2}. \tag{12}$$

Thus, the measurement of $V_{P\ nmo\ rms\ 1}$ and $V_{P\ nmo\ rms\ 2}$ allows to estimate the difference between δ_2 and δ_1 in both horizons A and B. The statistical distribution of these differences indicate that the most probable value is 0.015 (Fig. 11). Note that this result is independent of the analyzed horizon. Considering that δ (VTI) lies between δ_1 and δ_2, this average difference can be used to compute δ_1 and δ_2 as

$$\delta_1 = \delta - \frac{\delta_2 - \delta_1}{2} = 0.035 - \frac{0.015}{2} = 0.0275 \tag{13}$$

$$\delta_2 = \delta + \frac{\delta_2 - \delta_1}{2} = 0.035 + \frac{0.015}{2} = 0.0425. \tag{14}$$

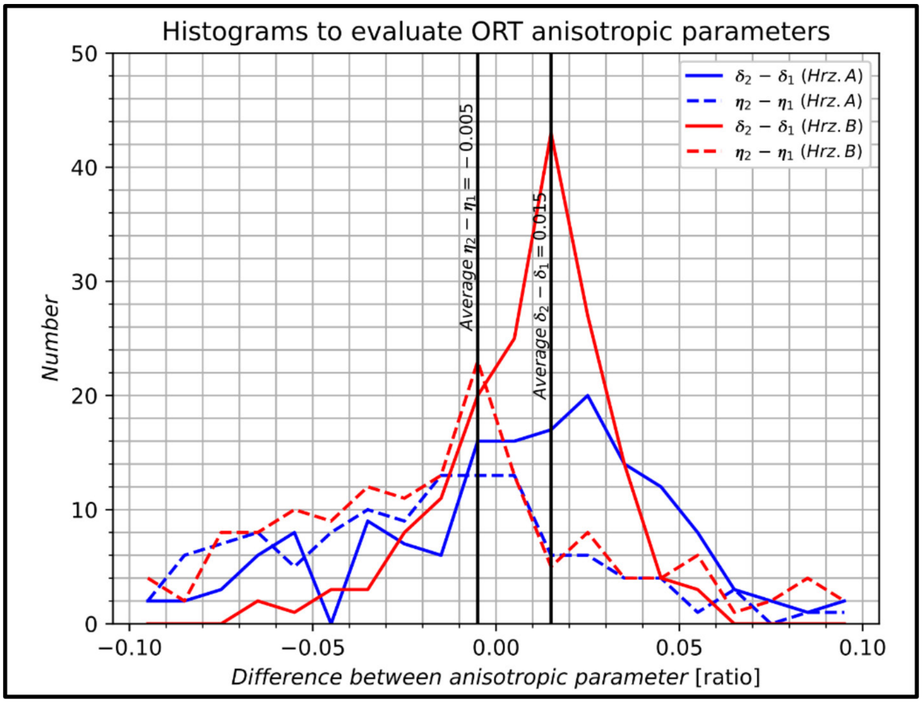

Figure 11. Histograms to evaluate useful differences between ORT anisotropic parameters.

The statistical distribution of the difference $\eta_{eff\,2}$ minus $\eta_{eff\,1}$ indicates that the most probable value is -0.005, independently of the analyzed horizon (Fig. 11). Then, the scalar values k_1 and k_2 to estimate $\eta_{eff\,1}$ and $\eta_{eff\,2}$ from η_{eff} are computed via

$$k_1^A = 1 - \frac{\eta_{eff\_2} - \eta_{eff\_1}}{2\eta_{eff}{}^A} = 1 + \frac{0.005}{2 \times 0.053} = 1.0476 \tag{15}$$

$$k_1^B = 1 - \frac{\eta_{eff\_2} - \eta_{eff\_1}}{2\eta_{eff}{}^B} = 1 + \frac{0.005}{2 \times 0.064} = 1.0391 \tag{16}$$

$$k_2^A = 1 + \frac{\eta_{eff\_2} - \eta_{eff\_1}}{2\eta_{eff}{}^A} = 1 - \frac{0.005}{2 \times 0.053} = 0.9524 \tag{17}$$

$$k_2^B = 1 + \frac{\eta_{eff\_2} - \eta_{eff\_1}}{2\eta_{eff}{}^B} = 1 - \frac{0.005}{2 \times 0.064} = 0.9609, \tag{18}$$

where supra-index A refers to horizon A and supra-index B refers to horizon B.

In both directions, the change of scalar values computed for horizons A and B is about 0.008. If this value is multiplied by an average η_{eff} of approximately 0.06, this change is negligible when compared to the most probable value of -0.005 for the difference between $\eta_{eff\,2}$ and $\eta_{eff\,1}$. Then

$$k_1 = \frac{k_1^A + k_1^B}{2} = 1.0434 \tag{19}$$

$$k_2 = \frac{k_2^A + k_2^B}{2} = 0.9566. \tag{20}$$

As a consequence, functions η_{eff_2} and η_{eff_1} can be computed as

$$\eta_{eff\_1} = k_1\,\eta_{eff} = 1.0434\,\eta_{eff} \tag{21}$$

$$\eta_{eff\_2} = k_2\,\eta_{eff} = 0.9566\ \eta_{eff}. \tag{22}$$

These effective functions are transformed to the interval η in time using the Dix formula to get η_1 and η_2. Using equation (2) for the minimum and maximum horizontal velocities directions, respectively

$$\varepsilon_1 = \delta_1 + \eta_1 + 2\delta_1\eta_1 \tag{23}$$

$$\varepsilon_2 = \delta_2 + \eta_2 + 2\delta_2\eta_2. \tag{24}$$

Next, using the estimated values for δ_1 and δ_2 from 13 and 14,

$$\varepsilon_1 = 0.0275 + \eta_1 + 0.055\ \eta_1 \tag{25}$$

$$\varepsilon_2 = 0.0425 + \eta_2 + 0.085\ \eta_2. \tag{26}$$

These expressions give an initial estimation for ε_1 and ε_2 (Fig. 12). From this starting point it is possible to simultaneously adjust these functions and estimate δ_3. First, effective $\varepsilon_{eff\,1}$ and $\varepsilon_{eff\,2}$ are computed and evaluated at horizon A, where

$$\varepsilon_{eff\_1}^A = 0.079 \tag{27}$$

$$\varepsilon_{eff\_2}^A = 0.089. \tag{28}$$

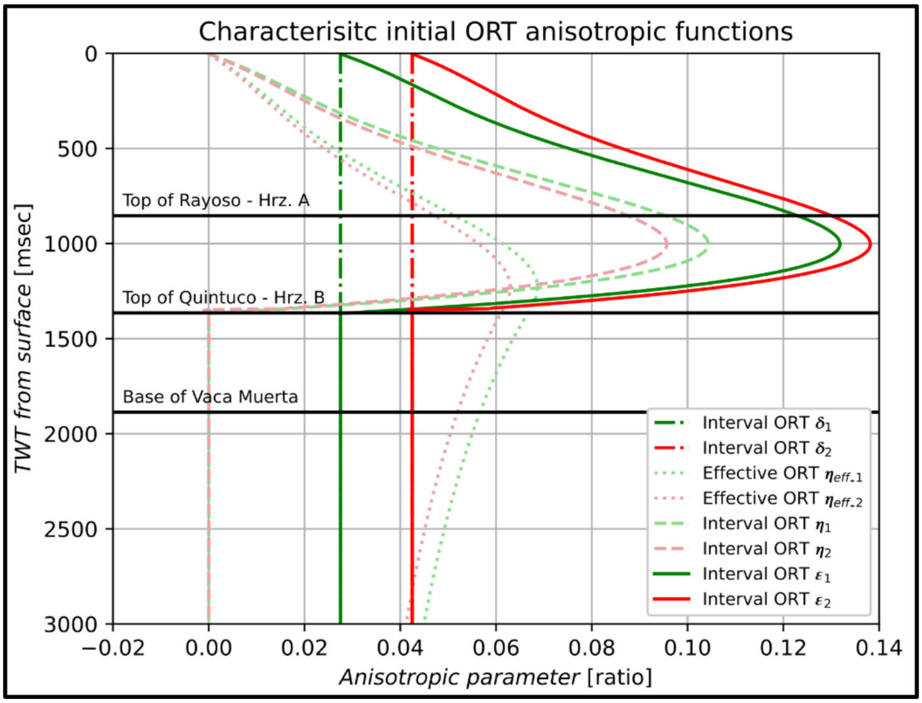

Figure 12. Characteristic initial ORT anisotropic functions.

Then on VTI PSTM COCA gathers, traveltimes t_j(offset, ϕ) that depend on the offset and the azimuth of propagation are measured at horizon A. There are two main reasons that explain why these traveltimes show a residual normal moveout that is not close to zero. The first one is related to the accuracy of $V_{P\ nmo\ rms}$ and η_{eff} fields used for the VTI PSTM stage and intrinsic limitations of this imaging strategy. As demonstrated by Alkhalifah, T., and Tsvankin, I. (1995), in a VTI media traveltimes depend on a fourth degree polynomial function of the offset. Consequently, a trend with those characteristics is computed and removed from the measured traveltimes to obtain values that do not depend on the offset: t_j(azimuth). The second residual effect is related to the way ε_{eff} changes with the azimuth, which is implicit in the variable ϕ. The relative difference of traveltimes $t_j(\phi)$ against its average value provides an estimator of the error in ε_{eff} (Fig. 13). Assuming that the average value of $\varepsilon_{eff\,1}$ and $\varepsilon_{eff\,2}$ is a reasonable estimation for ε_{eff}, then

$$\varepsilon_{eff}(\phi) = \varepsilon_{eff} + error\left(\varepsilon_{eff}(\phi)\right) \tag{29}$$

$$\varepsilon_{eff}(\phi) = \frac{\varepsilon_{eff\_1} + \varepsilon_{eff\_2}}{2} + \frac{t_j(\phi) - avg\left(t_j(\phi)\right)}{avg\left(t_j(\phi)\right)}. \tag{30}$$

Considering the effective properties on equation 6

$$\varepsilon_{eff}(\phi) = \varepsilon_{eff\_1}\sin^4\phi + \varepsilon_{eff\_2}\cos^4\phi + \left(2\varepsilon_{eff\_2} + \delta_{eff\_3}\right)\sin^2\phi\cos^2\phi. \tag{31}$$

Equalizing 30 and 31

$$\frac{t_j(\phi) - avg\left(t_j(\phi)\right)}{avg\left(t_j(\phi)\right)} = \varepsilon_{eff\_1}\left(\sin^4\phi - \frac{1}{2}\right) + \varepsilon_{eff\_2}\left(\cos^4\phi - \frac{1}{2} + 2\sin^2\phi\cos^2\phi\right) + \delta_{eff\_3}\sin^2\phi\cos^2\phi. \quad (32)$$

This expression can be used to find the corrections to the initial values of the parameters $\varepsilon_{eff\,1}$, $\varepsilon_{eff\,2}$, and $\varepsilon_{eff\,3}$ by adjusting the traveltimes measurements by least squares. Recall that the initial values of $\varepsilon_{eff\,1}$, $\varepsilon_{eff\,2}$ are given by 27 and 28, and $\varepsilon_{eff\,3}$ is taken equal to zero. Thus, if L is the vector of observations with homogenous weights, L0 is the estimated vector with initial parameters, C is the matrix of coefficients and X is the vector of corrections to the parameters, then

$$X = (C^tC)^{-1}C^t(L - L_0) = \begin{bmatrix} -0.00079 \\ -0.00018 \\ -0.01097 \end{bmatrix} \quad (33)$$

from where we obtain

$$\hat{\varepsilon}^A_{eff\_1} = 0.079 - 0.00079 = 0.07859 \quad (34)$$
$$\hat{\varepsilon}^A_{eff\_2} = 0.089 - 0.00018 = 0.08889 \quad (35)$$
$$\hat{\delta}^A_{eff\_3} = 0.000 - 0.01097 = -0.01097. \quad (36)$$

Figure 13 illustrates the relationship between the observations and the initial and adjusted model.

Then, effective properties in time can be corrected as follows

$$\hat{\varepsilon}_{eff\_1} = \frac{\hat{\varepsilon}^A_{eff\_1}}{\varepsilon^A_{eff\_1}}\varepsilon_{eff\_1} = \frac{0.07859}{0.079}\varepsilon_{eff\_1} = 0.9901\,\varepsilon_{eff\_1} \quad (37)$$
$$\hat{\varepsilon}_{eff\_2} = \frac{\hat{\varepsilon}^A_{eff\_2}}{\varepsilon^A_{eff\_2}}\varepsilon_{eff\_2} = \frac{0.08889}{0.089}\varepsilon_{eff\_2} = 0.9979\,\varepsilon_{eff\_2} \quad (38)$$
$$\hat{\delta}_{eff\_3} = \frac{\hat{\delta}^A_{eff\_3}}{\hat{\varepsilon}^A_{eff\_2}}\varepsilon_{eff\_2} = \frac{-0.01097}{0.08889}\varepsilon_{eff\_2} = -0.1234\,\varepsilon_{eff\_2}. \quad (39)$$

These corrected effective properties are transformed to interval properties in time: ε_1, ε_2, and δ_3 (Fig. 14). Then, these functions together with δ_1 and δ_2 from results 13 and 14 are converted to depth using the isotropic velocity model from each location to build the ORT models. Figure 4

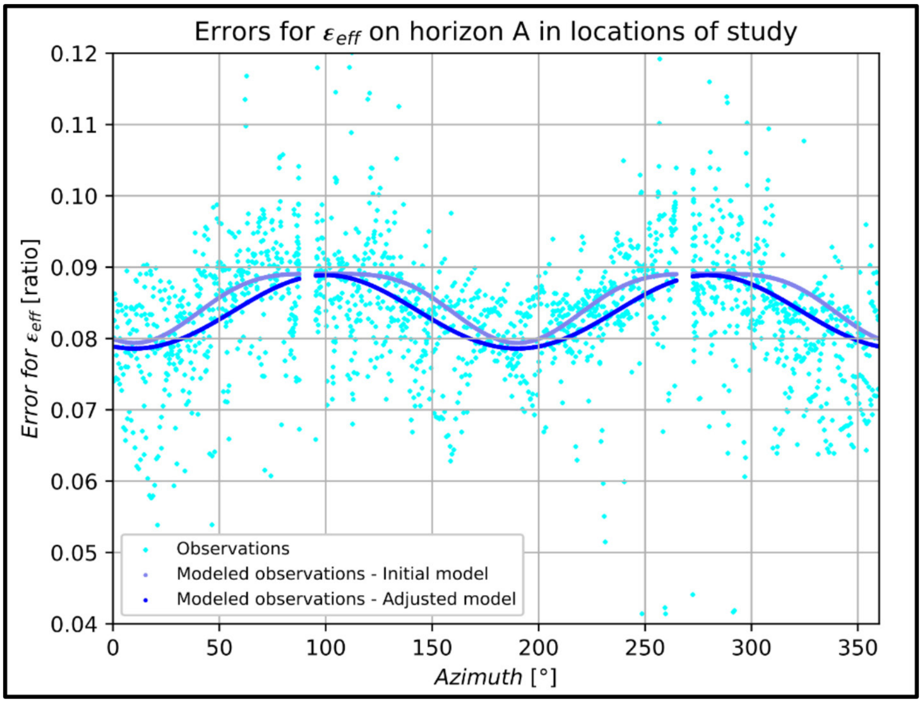

Figure 13. Errors for η_{eff} on horizon A in the locations of study. Observations and initial and adjusted models.

shows ε_1, ε_2, and δ_3 sections in depth for Location 1. Finally, these functions are used to compute $\delta(\phi)$ and $\varepsilon(\phi)$ using equations 5 and 6, thus obtaining expressions which are functions of the azimuth of the traces to be modeled.

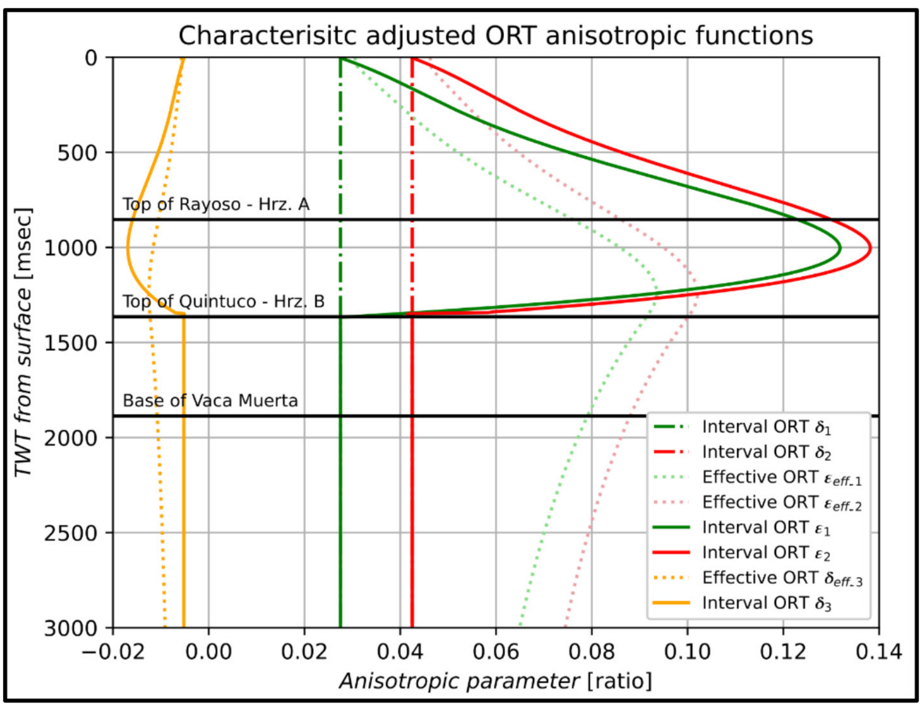

Figure 14. Characteristic adjusted ORT anisotropic functions.

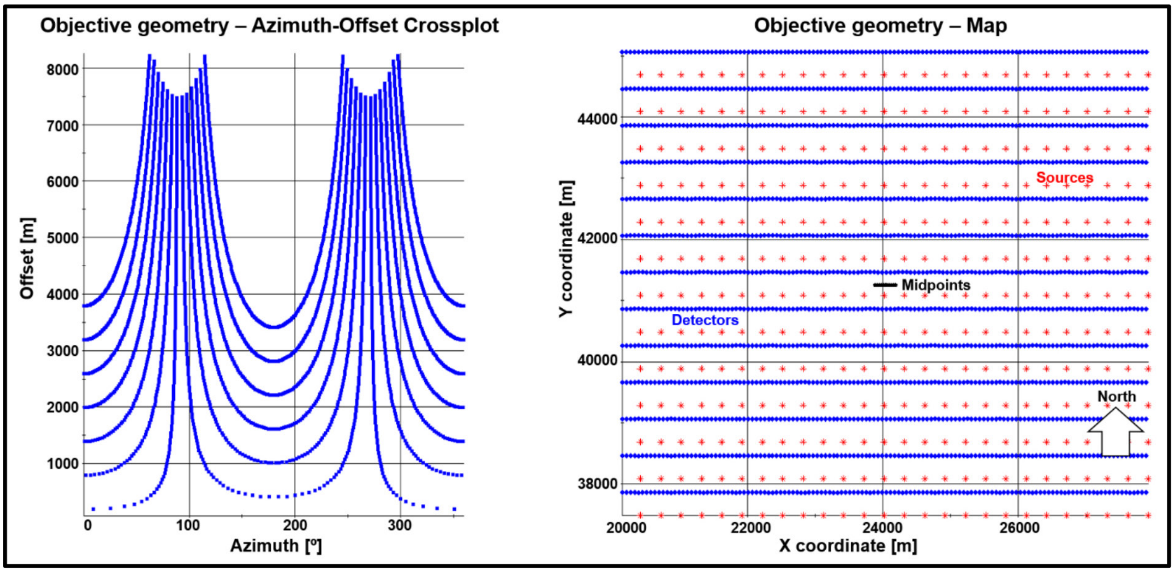

Figure 15. Objective geometry of Location 1.

Direct modeling and cross-correlation analysis

The estimated parameters are used to create 3D seismic synthetic responses for an isotropic scenario and VTI and ORT anisotropic models. The algorithm that is used in this stage is a wave equation modeling that predicts primaries and multiples reflections (Stork *et al.*, 2006). In this particular case, only the primaries reflections are modeled. This one-way propagator algorithm uses the previously produced properties in depth and a prior seismic image also in depth that is extracted from the corresponding PSDM cube and then propagated to the full area (Fig. 4).

The method also requires an objective geometry obtained from each COCA gather (Fig. 15). For the ORT case, this geometry is modeled by azimuth ranges every 10°, and the corresponding $\delta(\phi)$ and $\varepsilon(\phi)$ functions are computed for the central azimuth of each range.

After direct modeling, seismic traces are normal-moveout corrected using the same velocity function that is used for real gathers, making the visual assessment straightforward (Fig. 16). Also, each trace is cross-correlated against the stacked traces at a time window of (800-2100) msec to compute residual traveltimes that are conveniently averaged. This is carried out using offset ranges of 500 m as a first step, so the variability of the residual moveout in function of the offset can be statistically evaluated between the real seismic COCA gathers and isotropic, VTI and ORT synthetic results (Fig. 17). Secondly, the average is computed after removing the offset trend with a fourth degree polynomial fit and then averaging for azimuth ranges of 10° (Fig. 18). In this case, the variability of the residual moveout in function of the azimuth can be compared against the real and complete statistics of the VTI PSTM residual traveltimes that shows the Figure 3.

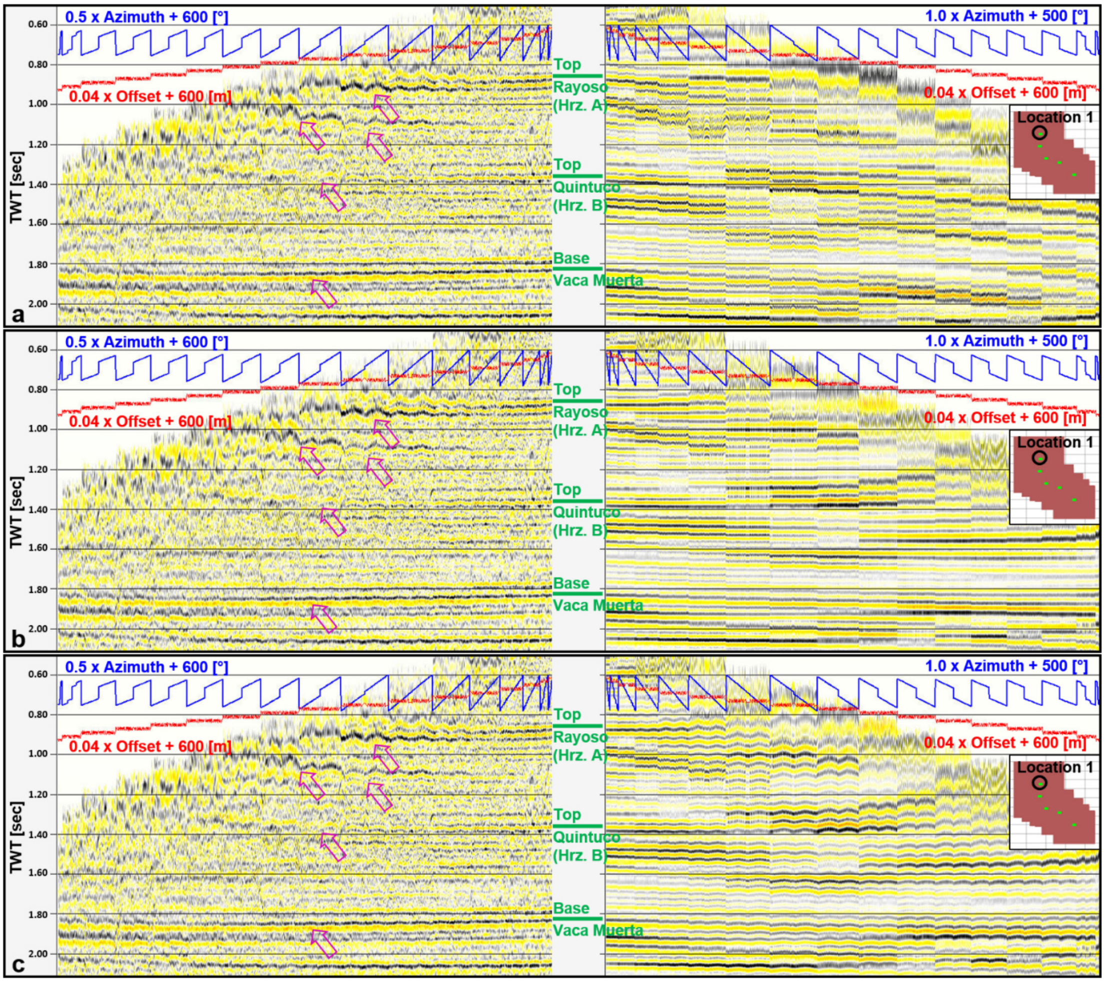

Figure 16. COCA gathers from Location 1. (a) Input to VTI PSTM (left). Isotropic direct modeling (right). (b) Input to VTI PSTM (left). VTI direct modeling (right). (c) Input to VTI PSTM (left). ORT direct modeling (right).

RESULTS

First results from direct modeling are shown in Location 1 (Fig. 16). A visual comparison against real data demonstrates that there is a consistent relationship between primaries of the isotropic results and real data on near offsets (Fig. 16a). This result implies that estimated vertical velocity VPz is accurate enough to explain the behavior of normal incidence reflections. However, the correlation with real data rapidly deteriorates when offsets increase. Traveltimes are too high for long offsets. This problem is solved to a certain degree when VTI parameters are considered in the modeling process (Fig. 16b). This fact indicates a clear presence of a VTI phenomenon in the area, demonstrating that the horizontal velocity VPh is higher than the vertical velocity VPz. The relationship between traveltimes and offsets are now more consistent between real and modeled data. Despite this clear improvement, those traveltimes patterns related with the azimuth are still not explained. The best correlation with real data is achieved when estimated ORT parameters are included to modify each corresponding $\delta(\phi)$ and $\varepsilon(\phi)$ functions (Fig. 16c). Consequently, the horizontal velocity V_{Ph} is not only higher than the vertical velocity V_{Pz}, but also depends on the direction of propagation, thus demonstrating the presence of orthorhombic (ORT) anisotropy. These results are confirmed by the statistical analysis of residual traveltimes. In both cases, when they are compared against the offsets (Fig. 17) and the azimuths (Fig. 18) distributions. The same results replicate for the rest of the locations of study (Locations 2, 3, 4, and 5). The ORT anisotropic model shows the highest correlation with real seismic data (Figs. 19 and 20).

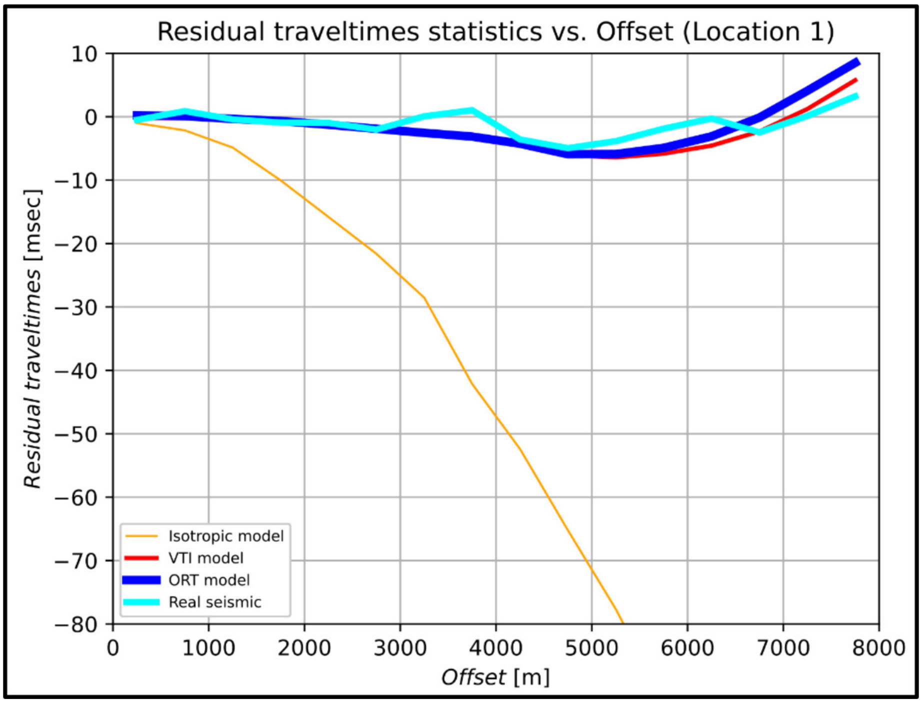

Figure 17. Location 1. Residual traveltimes statistics versus offset distribution.

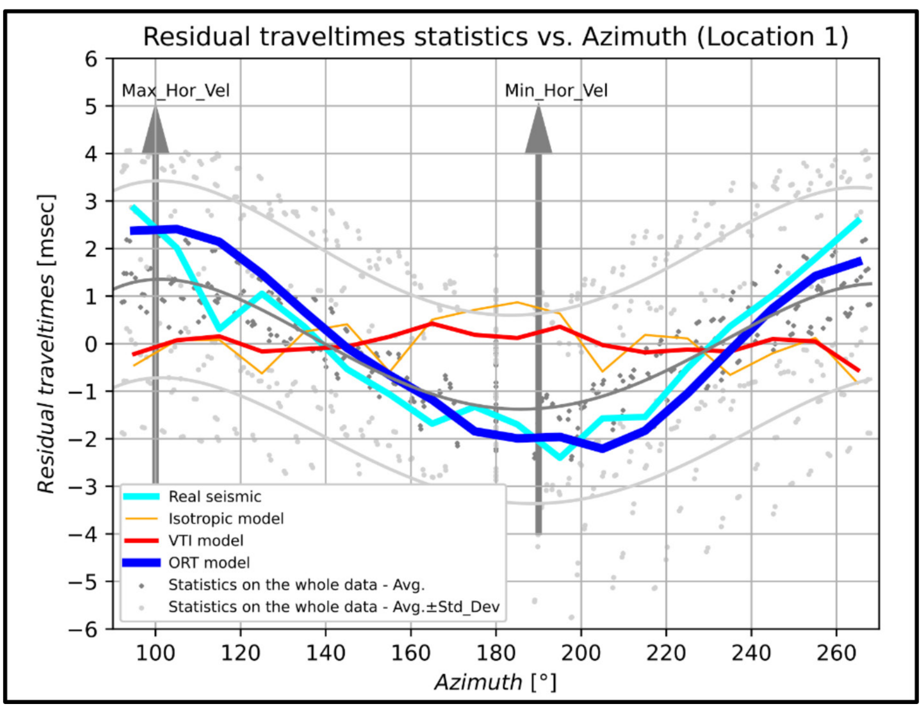

Figure 18. Location 1. Residual traveltimes statistics versus azimuth distribution. The offset trend was removed using a fourth-degree polynomial fit.

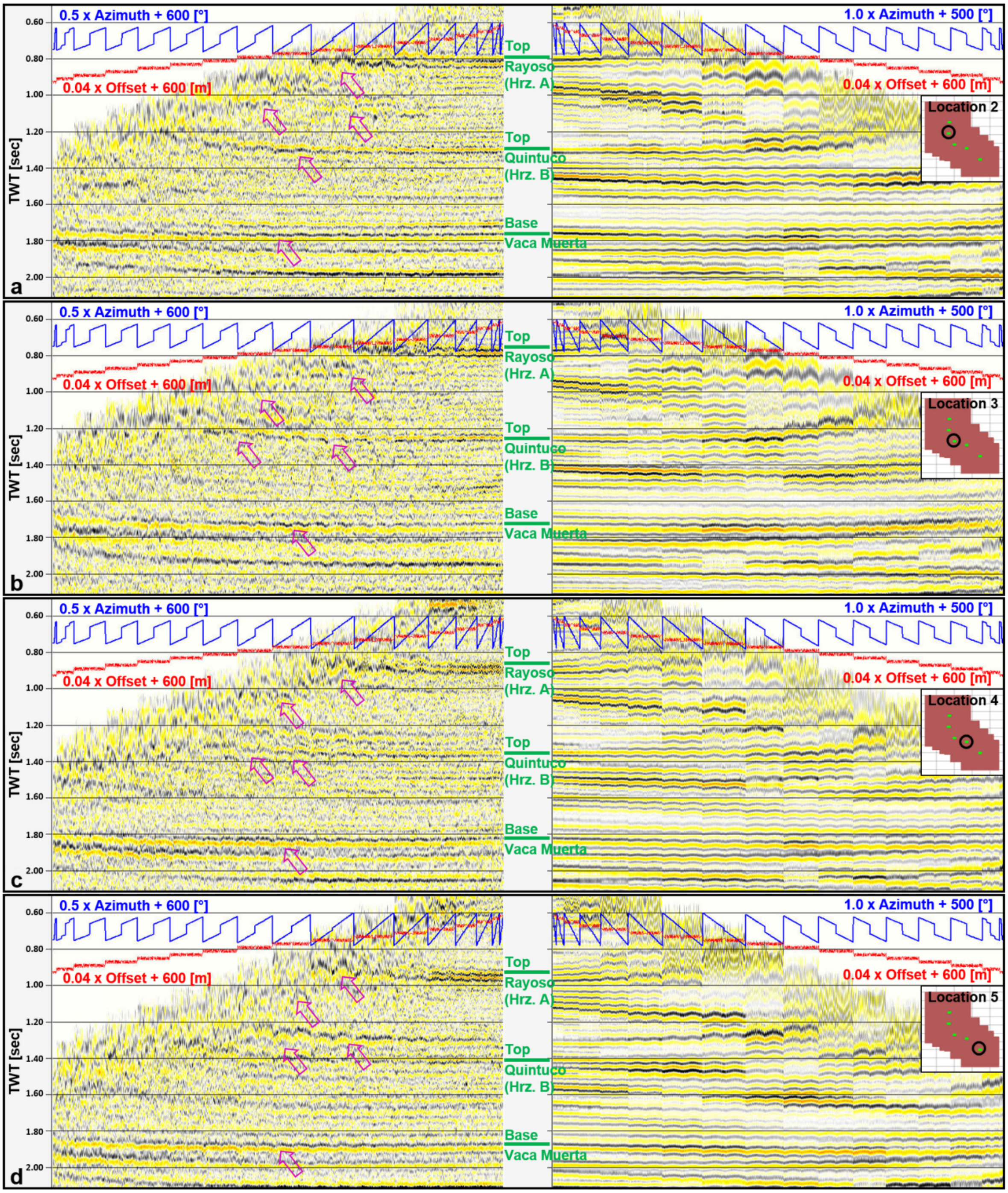

Figure 19. COCA gathers. Input to VTI PSTM (left). ORT direct modeling (right). (a) Location 2. (b) Location 3. (c) Location 4. (d) Location 5.

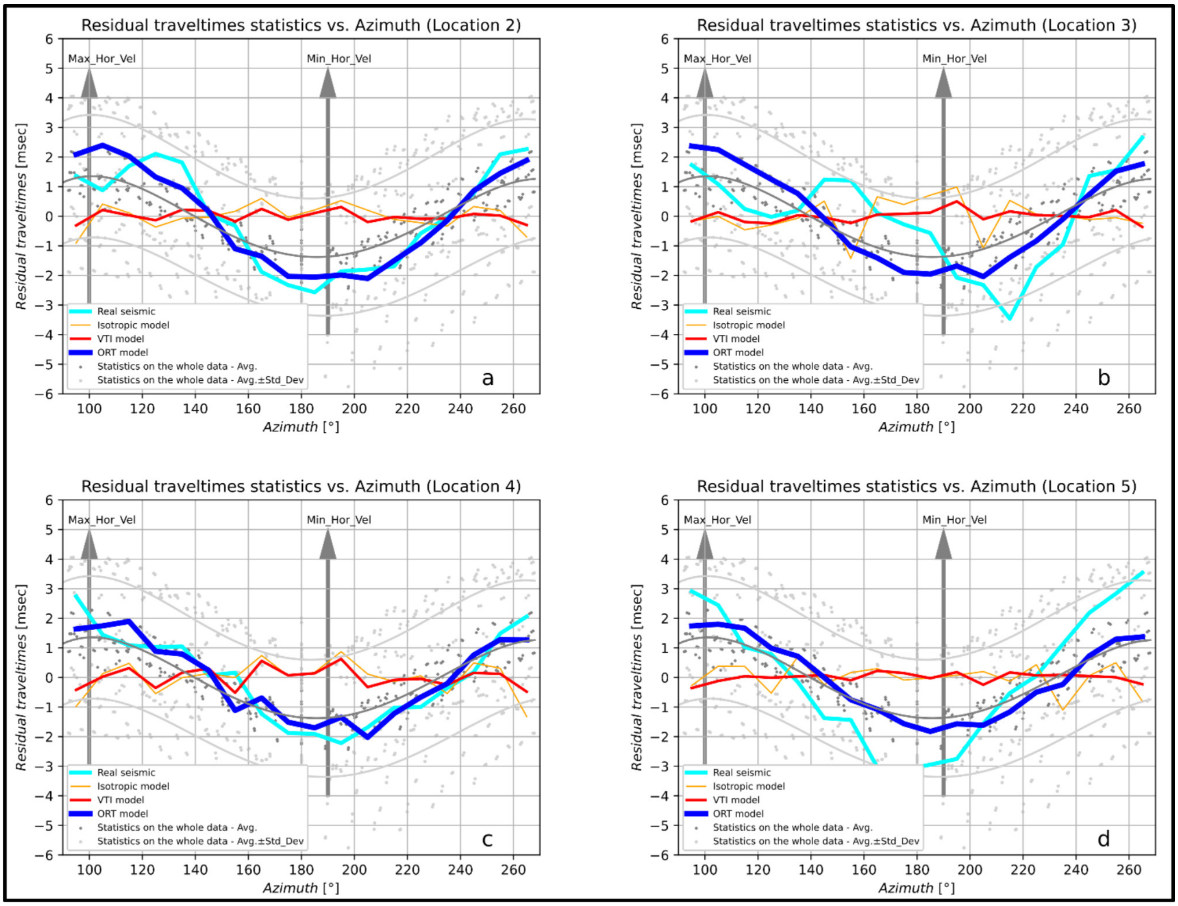

Figure 20. Residual traveltimes statistics versus azimuths distribution. The offset trend was removed using a fourth-degree polynomial fit. (a) Location 2. (b) Location 3. (c) Location 4. (d) Location 5.

CONCLUSIONS

Results demonstrate that a flat model without lateral changes of statics and velocities can produce synthetic preimage gathers that match those moveout patterns observed in real seismic data from the Embayment of the Neuquén Basin when an orthorhombic anisotropic model is considered. It is also shown that the residual normal moveout of real data can be properly handled to statistically estimate physically meaningful orthorhombic parameters. Well control is necessary for the accuracy of the vertical velocity VPz and the Thomsen´s parameter delta δ.

The synthetic results analysis shows that the effect of the orthorhombic phenomenon on primaries associated with geological formations of interest (i.e. Quintuco and Vaca Muerta) in this basin is significant, even for small angles of incidence, and even though highest anomalies of ORT parameters are above the top of the Quintuco formation.

From these results, a 3D synthetic model that covers the full area is necessary for studying the incidence of this behavior of seismic waves in issues like image focusing, amplitude distribution or residual traveltimes. All of them have a significant importance when surface seismic data is intended to be used for high-resolution studies in structural and stratigraphic interpretation, reservoir characterization, geomechanics and time-lapse analysis.

ACKNOWLEDGMENTS

The authors would like to first thank Tecpetrol S.A. for permission to publish the data examples contained within. We would also like to acknowledge the continuous support of Seismic Prospect S.R.L. to this project.

REFERENCES

Alkhalifah, T., and Tsvankin, I., 1995. Velocity analysis for transversely isotropic media. Geophysics, 60(5), pp. 1550-1566.

Benitez, P. E., 2019. Analysis of Velocity Variation with Azimuth (VVAZ) for Natural Fracture and Stress Characterization, Vaca Muerta Formation, Neuquén Basin, Argentina. Colorado School of Mines.

Bracaccini, C. I., 1970. Rasgos tectónicos de las acumulaciones mesozoicas en las provincias de Mendoza y Neuquén. Asociación Geológica Argentina, Revista 25: pp. 275-284. Buenos Aires.

Curia, D., Hanitzsch, C., Galikeev, T., Elia, R., and Davis, T., 2018. Multicomponent 3D-3C data acquisition and processing for characterization of Vaca Muerta Formation in Neuquén Basin, Argentina. The Leading Edge, 37(4), pp. 270-274.

Curia, D., Linares, L., Pare, A., Paris, M., and Corti, E., 2016. The use of walkaway and walkaround VSP surveys to characterize HTI and VTI anisotropy at the Vaca Muerta Formation. In SEG Technical Program Expanded Abstracts 2016 (pp. 5587-5591). Society of Exploration Geophysicists.

Dix, C. H., 1955. Seismic velocities from surface measurements. Geophysics, 20(1), pp. 68-86.

Grechka, V., and Tsvankin, I., 1999. 3-D moveout velocity analysis and parameter estimation for orthorhombic media. Geophysics, 64(3), pp. 820-837

Guzmán, C., Cristallini, E., and Bottesi, G., 2007. Contemporary stress orientations in the Andean retroarc between 34 S and 39 S from borehole breakout analysis. Tectonics, 26(3).

Heidbach, O., Rajabi, M., Reiter, K., Ziegler, M., & Wsm Team., 2016. World stress map database release 2016. GFZ Data Services, 10.

Hilburn, G., Pendharkar, A., Keller, W., Mott, R., Peinado, J., Jumper, A., and Kriechbaum, V., 2017. Fracture detection and reservoir characterization through high-resolution orthorhombic tomography for unconventional plays. In SEG Technical Program Expanded Abstracts 2017 (pp. 332-336). Society of Exploration Geophysicists.

Holcombe, H. T., Hong, T., Zhao, B., Salguero, E., Hallin, J., Wallace, M., and Zunino, E., 2014. Integrated seismic reservoir characterization of Vaca Muerta shale. In 2014 SEG Annual Meeting. Society of Exploration Geophysicists.

Jenner, E., 2011. Combining VTI and HTI anisotropy in prestack time migration: Workflow and data examples. The Leading Edge, 30(7), pp. 732-739.

Li, Y., Han, W., Chen, C. S., and Huang, T., 2012. Velocity model building for tilted orthorhombic depth imaging. In SEG Technical Program Expanded Abstracts 2012 (pp. 1-5). Society of Exploration Geophysicists.

Muzzio E. and María S., 2018. Caracterización sísmica de la Fm. Vaca Muerta en Cuenca Neuquina: ¿cómo aprovechar al máximo la información disponible, manejando sus incertidumbres? Análisis pre y post-drilling. In Congreso de Exploración y Desarrollo de Hidrocarburos. Simposio de Geofísica, volume 2018, pp. 1–18.

Neidell, N. S., and Taner, M. T., 1971. Semblance and other coherency measures for multichannel data. Geophysics, 36(3), pp. 482-497.

Sagasti, G., Ortiz, A., Hryb, D., Foster, M., and Lazzari, V., 2014. Understanding geological heterogeneity to customize field development: An example from the Vaca Muerta unconventional play, Argentina. In SPE/AAPG/SEG Unconventional Resources Technology Conference. Society of Exploration Geophysicists.

Soldo, J., Lanusse, I., Lorenzo, D., and Koremblit, M, 2017. A P-Wave Anisotropy Study for an Unconventional Play-Fracture Network Estimation in Vaca Muerta Fm., Argentina. In 79th EAGE Conference and Exhibition 2017 (Vol. 2017, No. 1, pp. 1-5). European Association of Geoscientists & Engineers.

Sosa, S. and Volonté, M., 2017. Migración en profundidad de dato sísmico terrestre: modelado de la superficie de referencia equivalente. In XXVIII Reunión Científica de la AAGG y III Simposio sobre Inversión y Procesamiento de Señales en Exploración Sísmica (La Plata, 2017)

Sosa S. and Volonté M., 2019. Orthorhombic PSDM for a valuable focused image of the Vaca Muerta Formation using a conventional land seismic acquisition. In Conference and Exhibition 2019. American Association of Petroleum Geologists.

Stork, C., Kapoor, J., Zhao, W., Dragoset, B., and Dingwall, K., 2006. Predicting and removing complex 3D surface multiples with WEM modeling - An alternative to 3D SRME for wide azimuth surveys? In SEG Technical Program Expanded Abstracts 2006 (pp. 2679-2683). Society of Exploration Geophysicists.

Thomsen, L., 1986. Weak elastic anisotropy. Geophysics, 51(10), pp. 1954-1966.

Tsvankin, I., 1997. Anisotropic parameters and P-wave velocity for orthorhombic media. Geophysics, 62(4), pp. 1292-1309.

Xie, Y., Birdus, S., Sun, J., and Notfors, C., 2012. Prestack depth imaging of multi-azimuth seismic data in the presence of orthorhombic anisotropy. ASEG Extended Abstracts, 2012(1), pp. 1-4.